

# An Efficient and Accurate Two-Stage Fourth-order Gas-kinetic Scheme for the Navier-Stokes Equations

Liang Pan<sup>a</sup>, Kun Xu<sup>a,b,\*</sup>, Qibing Li<sup>c</sup>, Jiequan Li<sup>d</sup>

<sup>a</sup>*Department of Mathematics, Hong Kong University of Science and Technology, Clear Water Bay, Kowloon, Hong Kong*

<sup>b</sup>*Department of Mechanical and Aerospace Engineering, Hong Kong University of Science and Technology, Clear Water Bay, Kowloon, Hong Kong*

<sup>c</sup>*School of Aerospace, Tsinghua University, Beijing 100084, China*

<sup>d</sup>*Institute of Applied Physics and Computational Mathematics, Beijing, 100088, China*

---

## Abstract

For computational fluid dynamics (CFD), the generalized Riemann problem (GRP) solver and the gas-kinetic kinetic scheme (GKS) provide a time-accurate flux function starting from a discontinuous piecewise linear flow distributions around each cell interface. With the use of time derivative of the flux function, a two-stage Lax-Wendroff-type (L-W for short) time stepping method has been recently proposed in the design of a fourth-order time accurate method [18]. In this paper, based on the same time-stepping method and the second-order GKS flux function [34], a fourth-order gas-kinetic scheme is constructed for the Euler and Navier-Stokes equations. In comparison with the formal one-stage time-stepping third-order gas-kinetic solver [21], the current fourth-order method not only reduces the complexity of the flux function, but also improves the accuracy of the scheme, even though the third- and fourth-order schemes have similar computation cost. Most importantly, the robustness of the fourth-order GKS is as good as the second-order one. Perfect numerical solutions can be obtained from the high Reynolds number boundary layer solutions to the hypersonic viscous heat conducting flow computations. Many numerical tests, including many difficult ones for the Navier-Stokes solvers, have been used to validate the current fourth-order method. Following the two-stage time-stepping framework, the one-stage third-order GKS can be easily extended to a fifth-order method with the usage of both first-order and second-order time derivatives of the flux function. The use of time-accurate flux function may have great impact on the development of higher-order CFD methods.

*Keywords:* two-stage Lax-Wendroff-type time stepping method, fourth-order gas-kinetic scheme, Navier-Stokes equations.

---



---

\*Corresponding author

*Email addresses:* panliangjlu@sina.com (Liang Pan), makxu@ust.hk (Kun Xu), lbq@tsinghua.edu.cn (Qibing Li), li\_jiequan@iapcm.ac.cn (Jiequan Li)

## 1. Introduction

To develop third and higher-order numerical methods has attracted great attention in recent decades. In comparison with second-order schemes, which were mostly developed in the 70s and 80s, the higher-order methods can provide more accurate solutions, but they are less robust and more complicated. There are many review papers and monographs about the current status of higher-orders schemes, which include the discontinuous Galerkin (DG) [6], essential non-oscillatory (ENO) [12], weighted essential non-oscillatory (WENO) [23],  $P_N P_M$  [8], multi-moment constrained method [13], and many others. Most of those methods use the Runge-Kutta time-stepping approach to achieve higher order temporal accuracy [10]. Based on the time-independent flux function of the Riemann solver [31], in order to achieve a fourth-order time accuracy, four-stage Runge-Kutta time stepping method has to be used. Moreover, the CFL number for those methods strongly depend on the order of the scheme, such as the DG method.

Recently, based on the time-dependent flux function of the generalized Riemann problem (GRP) [1, 2, 3], a two-stage fourth order time-accurate discretization was developed for Lax-Wendroff type (L-W for short) flow solvers, particularly applied for the hyperbolic conservation laws [18]. The reason for the success of a two-stage L-W type time stepping method in achieving a fourth-order time accuracy is solely due to the use of both flux function and its time derivative. In terms of the gas evolution model, the gas-kinetic scheme (GKS) provides a time accurate flux function as well, even though it depends on time through a much more complicated relaxation process from the kinetic to the hydrodynamic scale physics than the time-dependent flux function of GRP. This paper is about to construct a fourth-order time accurate gas-kinetic scheme (GKS) with the two-stage temporal discretization for the Euler and Navier-Stokes (NS) equations.

For the NS solutions, second-order and third-order gas-kinetic schemes have been constructed in the past years [34, 21, 16, 29]. The flux evaluation in the scheme is based on the time evolution of flow variables from an initial piece-wise discontinuous polynomials around each cell interface, where high-order spatial and temporal evolutions of a gas distribution function are coupled nonlinearly. In comparison with other high-order schemes, the GKS integrates the flux function over a time step analytically without employing the multi-stage Runge-Kutta time stepping techniques. However, with the one-stage gas evolution model, the formulation of GKS can become very complicated for the further improvement of the order of the scheme, such as the fourth-order scheme [22], especially for multidimensional computations. The two-stage L-W time stepping method in [18] provides a reliable framework to develop a fourth-order GKS with a second-order flux function. In this paper, we are going to present such a fourth-order GKS for the Euler and Navier-Stokes solutions. The current scheme can use a time step with CFL number on the order of 0.5. Most importantly, the current fourth-order GKS is as robust as the second-order method, which works perfectly from the subsonic to the hypersonic viscous heat conducting flows. Numerical tests show that the current scheme not only has the expected order of accuracy for the smooth flow, but also has favorable shock capturing property for the discontinuous solutions. As a further extension, the third-order flux function [28, 21, 24] can be also used to construct

two-stage fifth-order temporal accurate methods with the inclusion of both first-order and second-order time derivatives of the flux function. The detailed formulation is presented in the Appendix of this paper. Theoretically, this process for constructing even higher-order schemes can go forward continuously.

This paper is organized as follows. In Section 2, the general formulation for the two-stage temporal discretization is introduced. In Section 3, a fourth-order gas-kinetic scheme is presented based on the two-stage time discretization. Section 4 includes numerical examples to validate the current algorithm. The last section is drawing the conclusion. The extension for the construction of two-stage fifth-order schemes is given in Appendix.

## 2. Fourth-order temporal discretization

A two-stage fourth-order time-accurate discretization was developed for Lax-Wendroff flow solvers, particularly applied for hyperbolic equations with the generalized Riemann problem (GRP) solver [18]. Consider the following time-dependent equation,

$$\frac{\partial \mathbf{w}}{\partial t} = \mathcal{L}(\mathbf{w}), \quad (1)$$

with the initial condition at  $t_n$ , i.e.,

$$\mathbf{w}(t = t_n) = \mathbf{w}^n, \quad (2)$$

where  $\mathcal{L}$  is an operator for spatial derivative of flux. The time derivatives are obtained using the Cauchy-Kovalevskaya method,

$$\frac{\partial \mathbf{w}^n}{\partial t} = \mathcal{L}(\mathbf{w}^n), \quad \frac{\partial}{\partial t} \mathcal{L}(\mathbf{w}^n) = \frac{\partial}{\partial \mathbf{w}} \mathcal{L}(\mathbf{w}^n) \mathcal{L}(\mathbf{w}^n).$$

Introducing an intermediate state at  $t^* = t_n + \Delta t/2$ ,

$$\mathbf{w}^* = \mathbf{w}^n + \frac{1}{2} \Delta t \mathcal{L}(\mathbf{w}^n) + \frac{1}{8} \Delta t^2 \frac{\partial}{\partial t} \mathcal{L}(\mathbf{w}^n), \quad (3)$$

the corresponding time derivatives are obtained as well for the intermediate stage state,

$$\frac{\partial \mathbf{w}^*}{\partial t} = \mathcal{L}(\mathbf{w}^*), \quad \frac{\partial}{\partial t} \mathcal{L}(\mathbf{w}^*) = \frac{\partial}{\partial \mathbf{w}} \mathcal{L}(\mathbf{w}^*) \cdot \mathcal{L}(\mathbf{w}^*).$$

Then, the state  $\mathbf{w}$  can be updated with the following formula,

$$\mathbf{w}^{n+1} = \mathbf{w}^n + \Delta t \mathcal{L}(\mathbf{w}^n) + \frac{1}{6} \Delta t^2 \left( \frac{\partial}{\partial t} \mathcal{L}(\mathbf{w}^n) + 2 \frac{\partial}{\partial t} \mathcal{L}(\mathbf{w}^*) \right). \quad (4)$$

It can be proved that the above time stepping method with Eq.(3) and Eq.(4) provides a fourth-order time accurate solution for  $\mathbf{w}(t)$  at  $t = t_n + \Delta t$ . The details of the analysis can be found in [18]. Thus, based on a time accurate solution  $\partial \mathcal{L} / \partial t$ , a fourth-order temporal

accuracy can be achieved from the two-stage discretization of Eq.(1) through Eq.(3) and Eq.(4).

We apply this approach for conservation laws

$$\frac{\partial \mathbf{w}}{\partial t} + \frac{f(\mathbf{w})}{\partial x} = 0, \quad (5)$$

where  $\mathbf{w}$  is a conservative variable and  $f(\mathbf{w})$  is the corresponding flux, which includes all terms related to the viscous heat conducting flow. The semi-discrete form of a finite volume scheme for equations Eq.(5) can be written as

$$\frac{\partial \mathbf{w}_i}{\partial t} = \mathcal{L}_i(\mathbf{w}) = -\frac{1}{\Delta x_i}(\mathbf{f}_{i+1/2} - \mathbf{f}_{i-1/2}), \quad (6)$$

where  $\mathbf{w}_i$  are the cell averaged conservative variables of the cell  $I_i = [x_{i-1/2}, x_{i+1/2}]$ ,  $\mathbf{f}_{i+1/2}$  are the fluxes at the cell interface  $x = x_{i+1/2}$ , and  $\Delta x_i = x_{i+1/2} - x_{i-1/2}$ . A similar finite volume formulation can be obtained in two- and three-dimensional cases. Then (6) falls into the framework of the two-stage L-W time stepping.

### 3. A fourth-order gas-kinetic scheme

The similarity between the generalized Riemann problem (GRP) solver and the gas-kinetic scheme has been studied in [19]. In both schemes, the spatial and temporal accuracy are coupled through a generalized Lax-Wendroff-type procedure for the discontinuous cases, and a single stage time integration is used for the flux transport across a cell interface for the second-order schemes. In this section, a fourth-order gas-kinetic scheme from a second-order flux function will be constructed through a two-stage time discretization framework of Eq.(3) and Eq.(4) for the Euler and Navier-Stokes solutions.

#### 3.1. Second-order gas-kinetic flux solver

The two-dimensional BGK equation can be written as [4],

$$f_t + \mathbf{u} \cdot \nabla f = \frac{g - f}{\tau}, \quad (7)$$

where  $f$  is the gas distribution function,  $g$  is the corresponding equilibrium state, and  $\tau$  is the collision time. The collision term satisfies the compatibility condition

$$\int \frac{g - f}{\tau} \psi d\Xi = 0, \quad (8)$$

where  $\psi = (1, u, v, \frac{1}{2}(u^2 + v^2 + \xi^2))$ ,  $d\Xi = dudvd\xi^1 \dots d\xi^K$ ,  $K$  is the number of internal freedom, i.e.  $K = (4 - 2\gamma)/(\gamma - 1)$  for two-dimensional flows, and  $\gamma$  is the specific heat ratio. The conservative variables are denoted as  $W = (\rho, \rho U, \rho V, \rho E)$ . In the smooth region,

the gas distribution function can be expanded as

$$f = g - \tau D_{\mathbf{u}}g + \tau D_{\mathbf{u}}(\tau D_{\mathbf{u}})g - \tau D_{\mathbf{u}}[\tau D_{\mathbf{u}}(\tau D_{\mathbf{u}})g] + \dots,$$

where  $D_{\mathbf{u}} = \partial/\partial t + \mathbf{u} \cdot \nabla$ . By truncating on different orders of  $\tau$ , the corresponding macroscopic equations can be derived. For the Euler equations, the zeroth order truncation is taken, i.e.  $f = g$ . For the Navier-Stokes equations, the first order truncation is used,

$$f = g - \tau(ug_x + vg_y + g_t). \quad (9)$$

Based on the higher order truncations, the Burnett and super-Burnett equations can be obtained [5, 37, 35].

In order to update the flow variables, the flux is based on the integral solution of gas distribution function from the BGK equation at a cell interface,

$$f(x_{i+1/2}, t, u, v, \xi) = \frac{1}{\tau} \int_0^t g(x', y', t', u, v, \xi) e^{-(t-t')/\tau} dt' + e^{-t/\tau} f_0(-ut, y - vt, u, v, \xi), \quad (10)$$

where  $x_{i+1/2} = 0$  is the location of the cell interface,  $x = x' + u(t - t')$  and  $y = y' + v(t - t')$  are the trajectory of particles,  $f_0$  is the initial gas distribution function, and  $g$  is the corresponding equilibrium state. According to Eq.(10), the time dependent gas distribution function  $f(x_{i+1/2}, t, u, \xi)$  at the cell interface  $x_{i+1/2}$  can be expressed as [34, 36]

$$\begin{aligned} f(x_{i+1/2}, t, u, v, \xi) = & (1 - e^{-t/\tau})g_0 + ((t + \tau)e^{-t/\tau} - \tau)(\bar{a}_1u + \bar{a}_2v)g_0 \\ & + (t - \tau + \tau e^{-t/\tau})\bar{A}g_0 \\ & + e^{-t/\tau}g_r[1 - (\tau + t)(a_{1r}u + a_{2r}v) - \tau A_r]H(u) \\ & + e^{-t/\tau}g_l[1 - (\tau + t)(a_{1l}u + a_{2l}v) - \tau A_l](1 - H(u)). \end{aligned} \quad (11)$$

Based on the spatial reconstruction of macroscopic flow variables, which will be given in the next subsection, the conservative variables  $W_l$  and  $W_r$  on the left and right hand sides of a cell interface, and the corresponding equilibrium states  $g_l$  and  $g_r$ , can be determined. Their spatial derivatives in both normal and tangential directions, such as  $(a_{1l}, a_{1r}, a_{2l}, a_{2r})$ , are related to the normal and tangential derivatives of the initial macroscopic flow variables. The time derivatives  $(A_l, A_r)$  can be obtained from the requirement on the first-order Chapman-Enskog expansion, such as

$$\int g_l(a_{1l}u + a_{2l}v + A_l)\psi d\Xi = 0,$$

and

$$\int g_r(a_{1r}u + a_{2r}v + A_r)\psi d\Xi = 0.$$

Through the compatibility condition Eq.(8), the conservative variables  $W_0$  and the equi-

librium state  $g_0$  at the cell interface can be determined as follows,

$$\int \psi g_0 d\Xi = W_0 = \int_{u>0} \psi g_l d\Xi + \int_{u<0} \psi g_r d\Xi. \quad (12)$$

Then, with the spatial derivatives of macroscopic flow variables across and along a cell interface and the compatibility condition, the coefficients related to the spatial derivatives in the equilibrium state in Eq.(11), such as  $(\bar{a}_1, \bar{a}_2)$ , and its time derivative  $\bar{A}$ , can be fully obtained by,

$$\langle \bar{a}_1 \rangle = \frac{\partial \bar{W}}{\partial x}, \langle \bar{a}_2 \rangle = \frac{\partial \bar{W}}{\partial y}, \langle \bar{a}_1 u + \bar{a}_2 v + \bar{A} \rangle = 0, \quad (13)$$

where  $\langle \dots \rangle$  are the moments of the equilibrium gas distribution function  $g_0$ , and defined by

$$\langle \dots \rangle = \int g_0(\dots) \psi d\Xi.$$

More details of the gas-kinetic scheme can be found in [36].

### 3.2. Spatial reconstruction

The above time evolution solution is based on the high-order initial reconstruction for macroscopic flow variables, and the fifth-order WENO reconstruction is adopted in this study [14].

For one dimensional computation,  $W_l, W_r$  and  $W_0$  corresponding to the equilibrium states  $g_l, g_r$  and  $g_0$  in Eq.(11) can be constructed at the cell interface  $x_{i+1/2}$ . The spatial derivatives  $\partial W / \partial x$  are also given based on the reconstruction. Especially, for the determination of the equilibrium state  $g_0$  across the cell interface with a fifth-order of accuracy, the conservative variables around the cell interface can be expanded as

$$\bar{W}(x) = W_0 + S_1(x - x_*) + \frac{1}{2}S_2(x - x_*)^2 + \frac{1}{6}S_3(x - x_*)^3 + \frac{1}{24}S_4(x - x_*)^4.$$

With the following conditions,

$$\int_{I_{i+k}} \bar{W}(x) = W_{i+k}, k = -1, \dots, 2,$$

the derivatives are given by

$$\bar{W}_x = S_1 = \left[ -\frac{1}{12}(W_{i+2} - W_{i-1}) + \frac{5}{4}(W_{i+1} - W_i) \right] / \Delta x.$$

For two dimensional computation, the fifth-order Gauss quadrature is used to achieve the

accuracy in space

$$\frac{1}{\Delta y} \int_{y_{j-1/2}}^{y_{j+1/2}} F(W(x_{i+1/2}, y, t)) dy = \sum_{\ell=1}^k \omega_{\ell} F(W(x_{i+1/2}, y_{\ell}, t)), \quad (14)$$

where  $y_{\ell} \in [y_{j-1/2}, y_{j+1/2}]$ ,  $\ell = 1, \dots, 3$  are the Gauss quadrature points, and  $\omega_{\ell}$  are corresponding weights. Based on the tangential reconstruction, the tangential derivatives at each Gauss quadrature points can be obtained.

### 3.3. Two-stage gas-kinetic scheme

In this section, a two-stage fourth-order gas-kinetic scheme will be presented based on the time-dependent gas distribution function (11) at each cell interface.

For the gas-kinetic scheme, the gas evolution is a relaxation process from kinetic to hydrodynamic scale through the exponential function, and the corresponding flux is a complicated function of time. In order to obtain the time derivatives of the flux function at  $t_n$  and  $t_* = t_n + \Delta t/2$  with the correct physics, the flux function should be approximated as a linear function of time within a time interval. Let's first introduce the following notation,

$$\mathbb{F}_{i+1/2}(W^n, \delta) = \int_{t_n}^{t_n+\delta} F_{i+1/2}(W^n, t) dt = \int_{t_n}^{t_n+\delta} \int u f(x_{i+1/2}, t, u, v, \xi) du d\xi dt.$$

In the time interval  $[t_n, t_n + \Delta t]$ , the flux is expanded as the following linear form

$$F_{i+1/2}(W^n, t) = F_{i+1/2}^n + \partial_t F_{i+1/2}^n (t - t_n). \quad (15)$$

The coefficients  $F_{i+1/2}^n$  and  $\partial_t F_{i+1/2}^n$  can be determined as follows,

$$\begin{aligned} F_{i+1/2}(W^n, t_n) \Delta t + \frac{1}{2} \partial_t F_{i+1/2}(W^n, t_n) \Delta t^2 &= \mathbb{F}_{i+1/2}(W^n, \Delta t), \\ \frac{1}{2} F_{i+1/2}(W^n, t_n) \Delta t + \frac{1}{8} \partial_t F_{i+1/2}(W^n, t_n) \Delta t^2 &= \mathbb{F}_{i+1/2}(W^n, \Delta t/2). \end{aligned}$$

By solving the linear system, we have

$$\begin{aligned} F_{i+1/2}(W^n, t_n) &= (4\mathbb{F}_{i+1/2}(W^n, \Delta t/2) - \mathbb{F}_{i+1/2}(W^n, \Delta t)) / \Delta t, \\ \partial_t F_{i+1/2}(W^n, t_n) &= 4(\mathbb{F}_{i+1/2}(W^n, \Delta t) - 2\mathbb{F}_{i+1/2}(W^n, \Delta t/2)) / \Delta t^2. \end{aligned} \quad (16)$$

Similarly,  $F_{i+1/2}(W^*, t_*)$ ,  $\partial_t F_{i+1/2}(W^*, t_*)$  for the intermediate state can be constructed. For the two-dimensional computation, the corresponding fluxes in the  $y$ -direction can be obtained as well.

With these notations, the two-stage algorithm for both Euler and Navier-Stokes equations is given as follows

(i) With the initial reconstruction, update  $W_{ij}^*$  at  $t_* = t_n + \Delta t/2$  by

$$W_{ij}^* = W_{ij}^n - \frac{1}{\Delta x} [\mathbb{F}_{i+1/2,j}(W^n, \Delta t/2) - \mathbb{F}_{i-1/2,j}(W^n, \Delta t/2)] \\ - \frac{1}{\Delta y} [\mathbb{G}_{i,j+1/2}(W^n, \Delta t/2) - \mathbb{G}_{i,j-1/2}(W^n, \Delta t/2)],$$

and compute the fluxes and their derivatives by Eq.(16) for future use,

$$F_{i+1/2,j}(W^n, t_n), G_{i,j+1/2}(W^n, t_n), \partial_t F_{i+1/2,j}(W^n, t_n), \partial_t G_{i,j+1/2}(W^n, t_n).$$

(ii) Reconstruct intermediate value  $W_{ij}^*$ , and compute

$$\partial_t F_{i+1/2,j}(W^*, t_*), \partial_t G_{i,j+1/2}(W^*, t_*),$$

where the derivatives are determined by Eq.(16) in the time interval  $[t_*, t_* + \Delta t]$ .

(iii) Update  $W_{ij}^{n+1}$  by

$$W_{ij}^{n+1} = W_{ij}^n - \frac{\Delta t}{\Delta x} [\mathcal{F}_{i+1/2,j}^n - \mathcal{F}_{i-1/2,j}^n] - \frac{\Delta t}{\Delta y} [\mathcal{G}_{i,j+1/2}^n - \mathcal{G}_{i,j-1/2}^n],$$

where  $\mathcal{F}_{i+1/2,j}^n$  and  $\mathcal{G}_{i,j+1/2}^n$  are the numerical fluxes and expressed as

$$\mathcal{F}_{i+1/2,j}^n = F_{i+1/2,j}(W^n, t_n) + \frac{\Delta t}{6} [\partial_t F_{i+1/2,j}(W^n, t_n) + 2\partial_t F_{i+1/2,j}(W^*, t_*)], \\ \mathcal{G}_{i,j+1/2}^n = G_{i,j+1/2}(W^n, t_n) + \frac{\Delta t}{6} [\partial_t G_{i,j+1/2}(W^n, t_n) + 2\partial_t G_{i,j+1/2}(W^*, t_*)].$$

For each flux, the Gaussian quadratures Eq.(14) are used.

#### 4. Numerical tests

In this section, numerical tests for both inviscid and viscous flows will be presented to validate our numerical scheme. For the inviscid flow, the collision time  $\tau$  takes

$$\tau = \epsilon \Delta t + C \left| \frac{p_l - p_r}{p_l + p_r} \right| \Delta t,$$

where  $\epsilon = 0.05$  and  $C = 1$ . For the viscous flow, we have

$$\tau = \frac{\mu}{p} + C \left| \frac{p_l - p_r}{p_l + p_r} \right| \Delta t,$$

where  $p_l$  and  $p_r$  denote the pressure on the left and right sides of the cell interface,  $\mu$  is the viscous coefficient, and  $p$  is the pressure at the cell interface. In smooth flow regions, it will reduce to  $\tau = \mu/p$ . The ratio of specific heats takes  $\gamma = 1.4$ . The reason for including



artificial dissipation through the additional term in the particle collision time is to enlarge the kinetic scale physics in the discontinuous region for the construction of a numerical shock structure through the particle free transport and inadequate particle collision.

For the smooth flow, the WENO reconstruction can be used directly on the conservative flow variables. For the flow with strong discontinuity, the characteristic variables can be used in the reconstruction. Based on  $A_{i+1/2,j} = (\partial F / \partial W)_{W=W^*}$ , where  $W$  are the conservative variables,  $F(W)$  are the corresponding fluxes, and  $W^* = (W_{i,j} + W_{i+1,j})/2$ , the cell averaged and point conservative values can be projected into the characteristic field by  $\omega = RW$ , where  $R$  is the matrix corresponding to right eigenvectors of  $A$ . The reconstruction scheme is applied on the characteristic variables  $\omega$ . With the reconstructed polynomials for characteristic variables, the conservative flow variables can be recovered by the inverse projection.

#### 4.1. Accuracy tests

The first case is the advection of density perturbation, and the initial condition is set as follows

$$\rho(x) = 1 + 0.2 \sin(\pi x), \quad U(x) = 1, \quad p(x) = 1, \quad x \in [0, 2].$$

The periodic boundary condition is adopted, and the analytic solution is

$$\rho(x, t) = 1 + 0.2 \sin(\pi(x - t)), \quad U(x, t) = 1, \quad p(x, t) = 1.$$

In the computation, a uniform mesh with  $N$  points is used. As analyzed in the section before, with the fifth-order spatial reconstruction, the leading truncation error for the fourth-order GKS is  $O(\Delta x^5 + \Delta t^4)$ . In these tests, a fixed CFL number  $CFL = 0.4$  is used for different meshes. The  $L^1$  and  $L^2$  errors and orders at  $t = 2$  are presented in Table.1. The fifth order accuracy can be kept until the mesh  $N = 640$ . As a comparison, with the original second-order GKS, the leading error is on the order of  $O(\Delta x^5 + \Delta t^2)$ . With the identical spatial reconstruction and CFL number  $CFL = 0.4$ , only a second-order accuracy can be achieved. To show the order of accuracy, a small CFL number  $CFL = 0.1$  is used. The  $L^1$  and  $L^2$  errors and orders at  $t = 2$  are presented in Table.2. The fifth order accuracy can be kept at the beginning. With the mesh refinement, the temporal error becomes the dominant one and the accuracy reduces to a second order method.

The next test is the isotropic vortex propagation problem. The mean flow is  $(\rho, U, V, p) = (1, 1, 1, 1)$ , and an isotropic vortex is added to the mean flow, i.e., with perturbation in  $u, v$  and temperature  $T = p/\rho$ , and no perturbation in entropy  $S = p/\rho^\gamma$ . The perturbation is given by

$$(\delta U, \delta V) = \frac{\epsilon}{2\pi} e^{\frac{(1-r^2)}{2}} (-y, x), \quad \delta T = -\frac{(\gamma-1)\epsilon^2}{8\gamma\pi^2} e^{1-r^2}, \quad \delta S = 0,$$

where  $r^2 = x^2 + y^2$  and the vortex strength  $\epsilon = 5$ . The computational domain is  $[-5, 5] \times [-5, 5]$ , the periodic boundary conditions are imposed on the boundaries in both  $x$  and

mesh	$L^1$ error	convergence order	$L^2$ error	convergence order
20	4.4759E-004		3.7653E-004	
40	1.3764E-005	5.0231	1.1504E-005	5.0324
80	4.2791E-007	5.0075	3.4744E-007	5.0493
160	1.3354E-008	5.0018	1.0644E-008	5.0286
320	4.1722E-010	5.0003	3.2940E-010	5.0140
640	1.3039E-011	4.9998	1.0250E-011	5.0060
1280	4.5156E-013	4.8517	3.5536E-013	4.8502

Table 1: Accuracy test for the advection of density perturbation by the fourth-order GKS.

mesh	$L^1$ error	convergence order	$L^2$ error	convergence order
20	4.5797E-004		3.7856E-004	
40	1.3994E-005	5.0322	1.1735E-005	5.0116
80	1.0709E-006	3.7078	8.5971E-007	3.7708
160	2.5659E-007	2.0613	2.0167E-007	2.0918
320	6.4243E-008	1.9978	5.0455E-008	1.9989

Table 2: Accuracy test for the advection of density perturbation by the second-order GKS.

mesh	$L^1$ error	convergence order	$L^\infty$ error	convergence order
$20 \times 20$	1.98E-3		3.79E-2	
$40 \times 40$	1.69E-4	3.55	8.08E-3	2.23
$80 \times 80$	8.92E-6	4.24	4.10E-4	4.30
$160 \times 160$	2.31E-7	5.27	5.29E-6	6.28
$320 \times 320$	7.40E-9	4.96	2.09E-7	4.66
$640 \times 640$	2.76E-10	4.74	7.09E-9	4.88

Table 3: Accuracy of the fourth-order GKS for the isentropic vortex propagation at time  $t = 10$

$y$  directions. The exact solution is the perturbation which propagates with the velocity  $(1, 1)$ . The  $L^1$  and  $L^\infty$  errors and orders at  $t = 10$  with  $N \times N$  uniform mesh cells are presented in Table 3, which shows that the expected accuracy can be also achieved for the two dimensional computation.

#### 4.2. One dimensional Riemann problems

For one-dimensional case, two Riemann problems are considered. The first one is the Sod problem. The computational domain is  $[0, 1]$  with 100 uniform mesh points and with non-reflected boundary condition on both ends. The initial condition is given by

$$(\rho, U, p) = \begin{cases} (1, 0, 1), & 0 < x < 0.5, \\ (0.125, 0, 0.1), & 0.5 < x < 1. \end{cases}$$

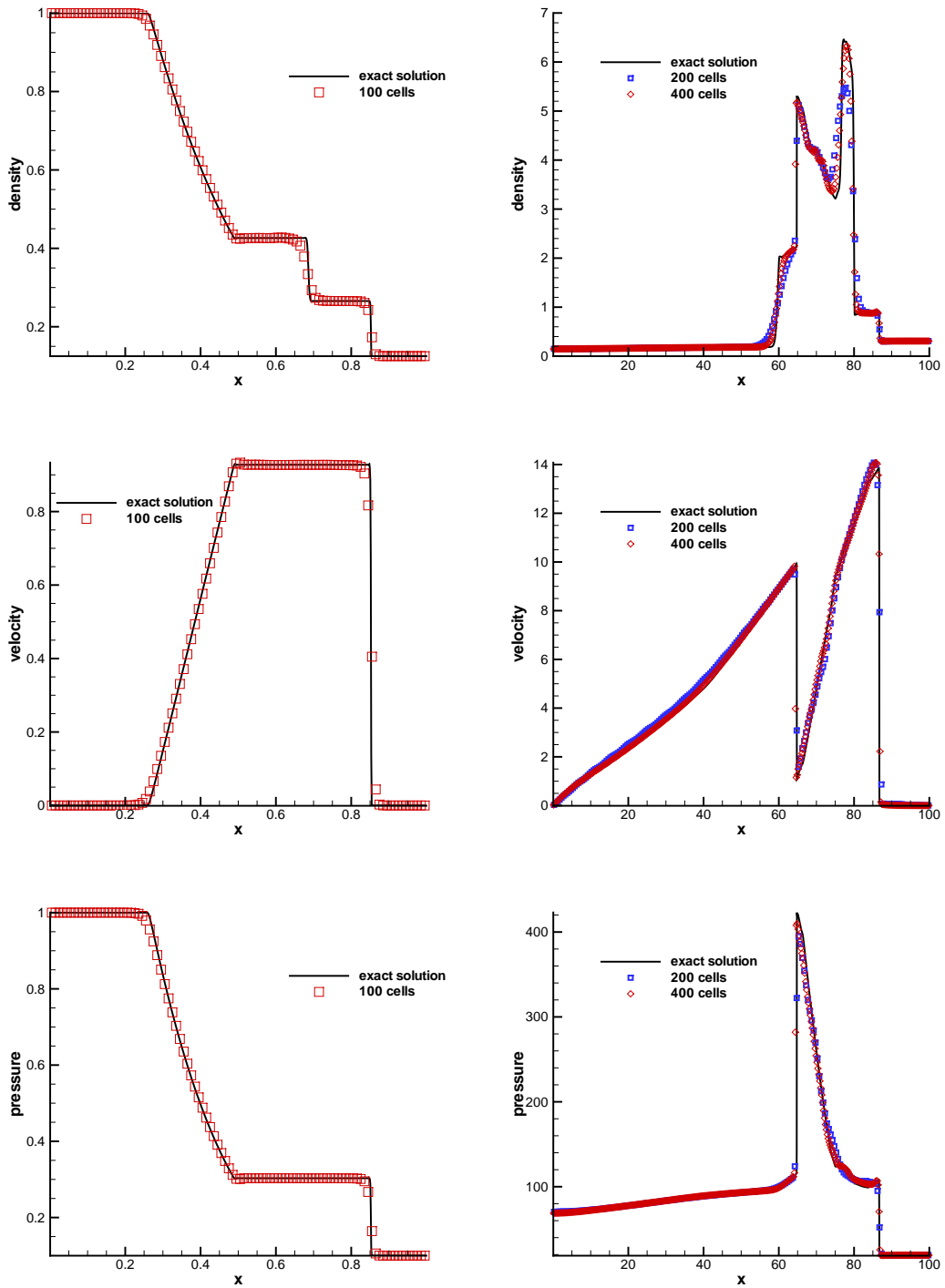


Figure 1: Sod problem (left): the density, velocity and pressure distributions at  $t=0.2$  with 100 cells, and blast wave problem (right): the density, velocity and pressure distributions at  $t = 3.8$  with 200 and 400 cells.

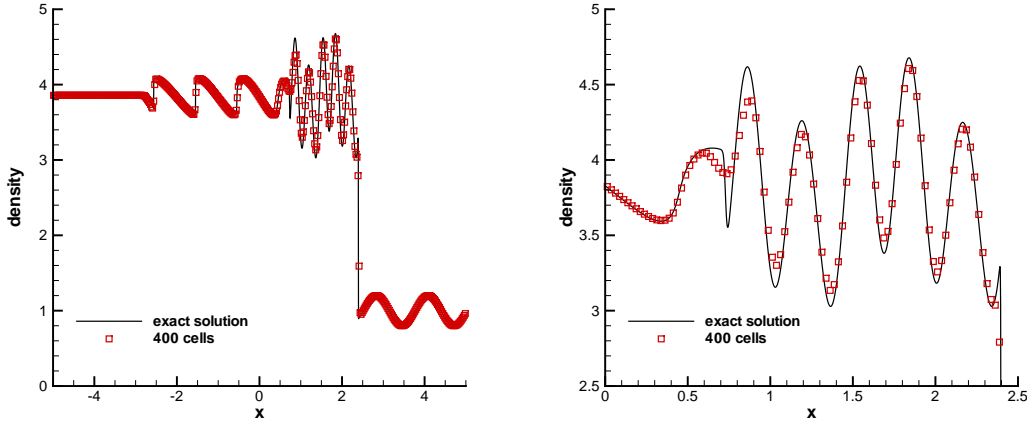


Figure 2: Shu-Osher shock acoustic-wave interaction. Density distributions at  $t = 1.8$  with 400 cells.

The second one is the Woodward-Colella blast wave problem [33]. The computational domain is  $[0, 100]$  with 200 and 400 uniform mesh points. The reflected boundary conditions are imposed on both ends. The initial conditions are given as follows,

$$(\rho, U, p) = \begin{cases} (1, 0, 1000), & 0 \leq x < 10, \\ (1, 0, 0.01), & 10 \leq x < 90, \\ (1, 0, 100), & 90 \leq x \leq 100. \end{cases}$$

The density, velocity, and pressure distributions for the fourth-order GKS and the exact solutions are presented in Fig.1 for the Sod problem at  $t = 0.2$  and for the blast wave problem at  $t = 3.8$ . The numerical results agree well with the exact solutions. The scheme can resolve the wave profiles well, particularly for the local extreme values.

In the one-dimensional case, another standard test case is the Shu-Osher shock acoustic interaction [30]. The computational domain is  $[-5, 5]$  and the flow field is initialized as

$$(\rho, U, p) = \begin{cases} (3.857134, 2.629369, 10.33333), & x \leq -4, \\ (1 + 0.2 \sin(5x), 0, 1), & -4 < x. \end{cases}$$

The computed density profile with 400 mesh points at  $t = 1.8$  is shown in Fig.2.

The stability for the current scheme is tested by the Sod problem. The velocity profiles with different  $CFL$  numbers from 0.2 to 0.7, are shown in Fig.3. The scheme is basically stable under the conventional  $CFL$  condition. The waves profiles can be well resolved at a  $CFL$  number around 0.5. In the following numerical tests, without special statement, the  $CFL$  number takes a fixed value of 0.4.

#### 4.3. Two-dimensional Riemann problems

In the following, two examples of two-dimensional Riemann problems are considered, which involve the interactions of shocks, the interaction of shocks with vortex sheets, and

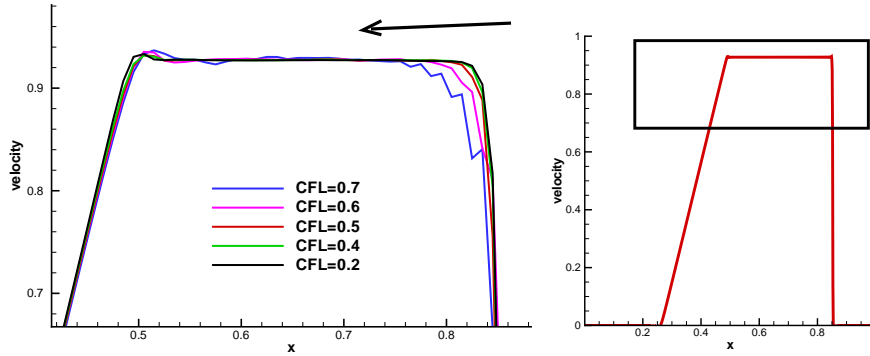


Figure 3: The stability test for the Sod problem.

the interaction of vortices [17, 20, 11]. The computational domain is  $[0, 1] \times [0, 1]$ , and the non-reflecting boundary conditions are used in all boundaries. The initial conditions for the first problem are

$$(\rho, U, V, p) = \begin{cases} (1.5, 0, 0, 1.5), & x > 0.5, y > 0.5, \\ (0.5323, 1.206, 0, 0.3), & x < 0.5, y > 0.5, \\ (0.138, 1.206, 1.206, 0.029), & x < 0.5, y < 0.5, \\ (0.5323, 0, 1.206, 0.3), & x > 0.5, y < 0.5. \end{cases}$$

Four initial shock waves interact with each other and result in a more complicated pattern. The density distribution and the local enlargement are given at  $t = 0.4$  in Fig.4 with  $400 \times 400$  and  $800 \times 800$  mesh points. From the analysis in [17], the initial shock wave  $S_{23}^-$  bifurcates at the trip point into a reflected shock wave, a Mach stem, and a slip line. The reflected shock wave interacts with the shock wave  $S_{12}^-$  to produce a new shock. The small scale flow structures are well captured by the current scheme.

The initial conditions for the second case are

$$(\rho, U, V, p) = \begin{cases} (1, 0.1, 0.1, 1), & x > 0.5, y > 0.5, \\ (0.5197, -0.6259, 0.1, 0.4), & x < 0.5, y > 0.5, \\ (0.8, 0.1, 0.1, 0.4), & x < 0.5, y < 0.5, \\ (0.5197, 0.1, -0.6259, 0.4), & x > 0.5, y < 0.5. \end{cases}$$

This case is to simulate the interaction of the rarefaction waves and the vortex-sheets. The density distribution at  $t = 0.4$  and the local enlargement are given in Fig.5 with  $600 \times 600$  and  $1000 \times 1000$  mesh points. The roll-up is well captured by the current scheme.

On the computational cost, the above two-dimensional Riemann problems are tested again. As a reference, the CPU times for different schemes are obtained with  $100 \times 100$  cells and 10 time steps with Intel Core i7-4770 CPU @ 3.40GHz. Based on the same WENO reconstruction, the CPU times for the second-order GKS [34], the single stage third-order

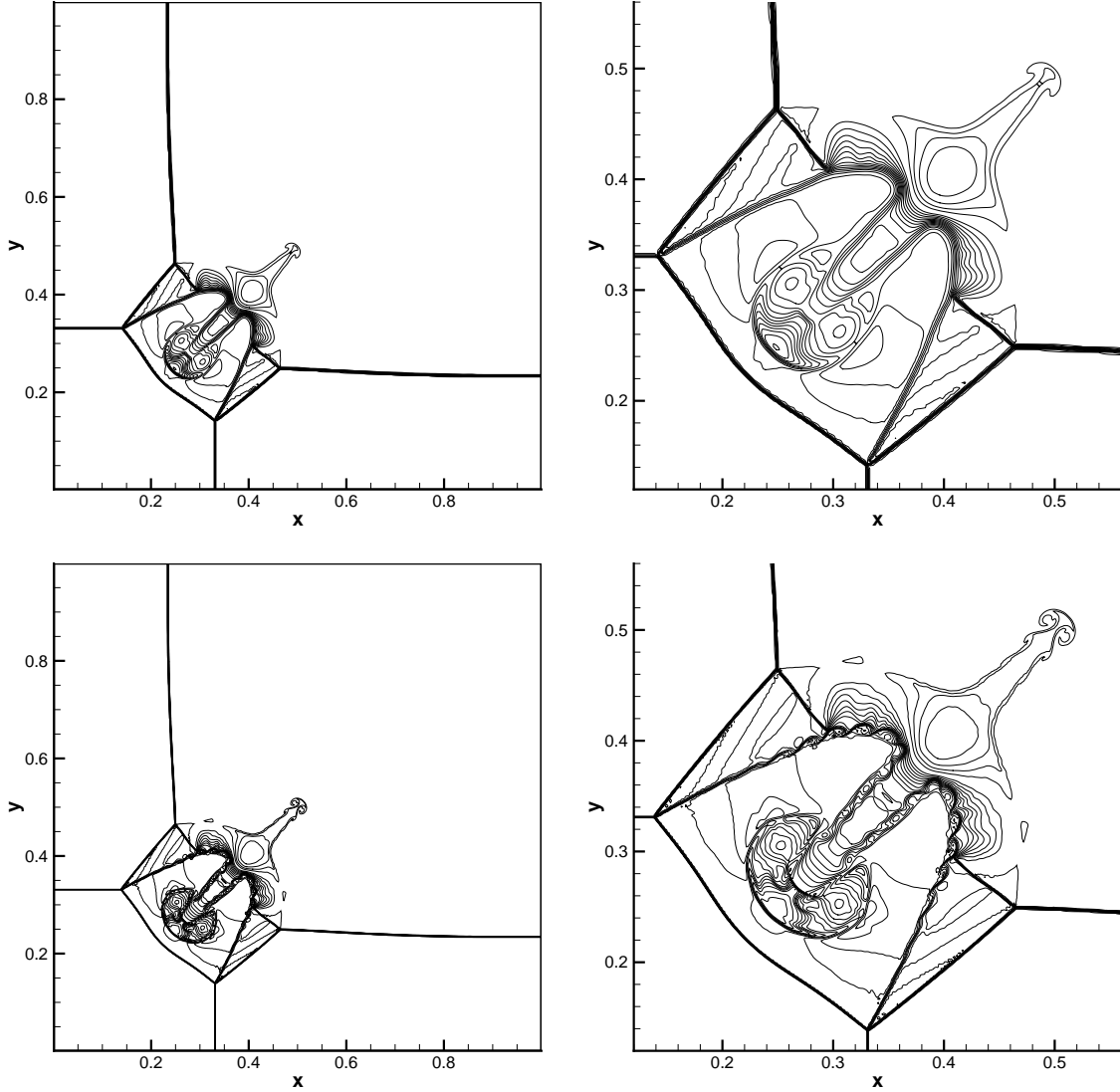


Figure 4: The density distribution for the first two-dimensional Riemann problem at  $t = 0.3$  with  $400 \times 400$  (top) and  $800 \times 800$  (bottom) mesh points.

GKS [21, 24], and the current two-stage fourth-order GKS are given in Table 4, where both conservative and characteristic reconstructions are used.

variable	2nd-order GKS	3rd-order GKS	4th-order GKS
conservative	0.704893s	1.24681s	1.95370s
characteristic	0.842873s	1.38178s	2.20566s

Table 4: The test of the computational cost for different schemes.

For the fourth-order GKS, the computational cost is about 3 times of that of second-

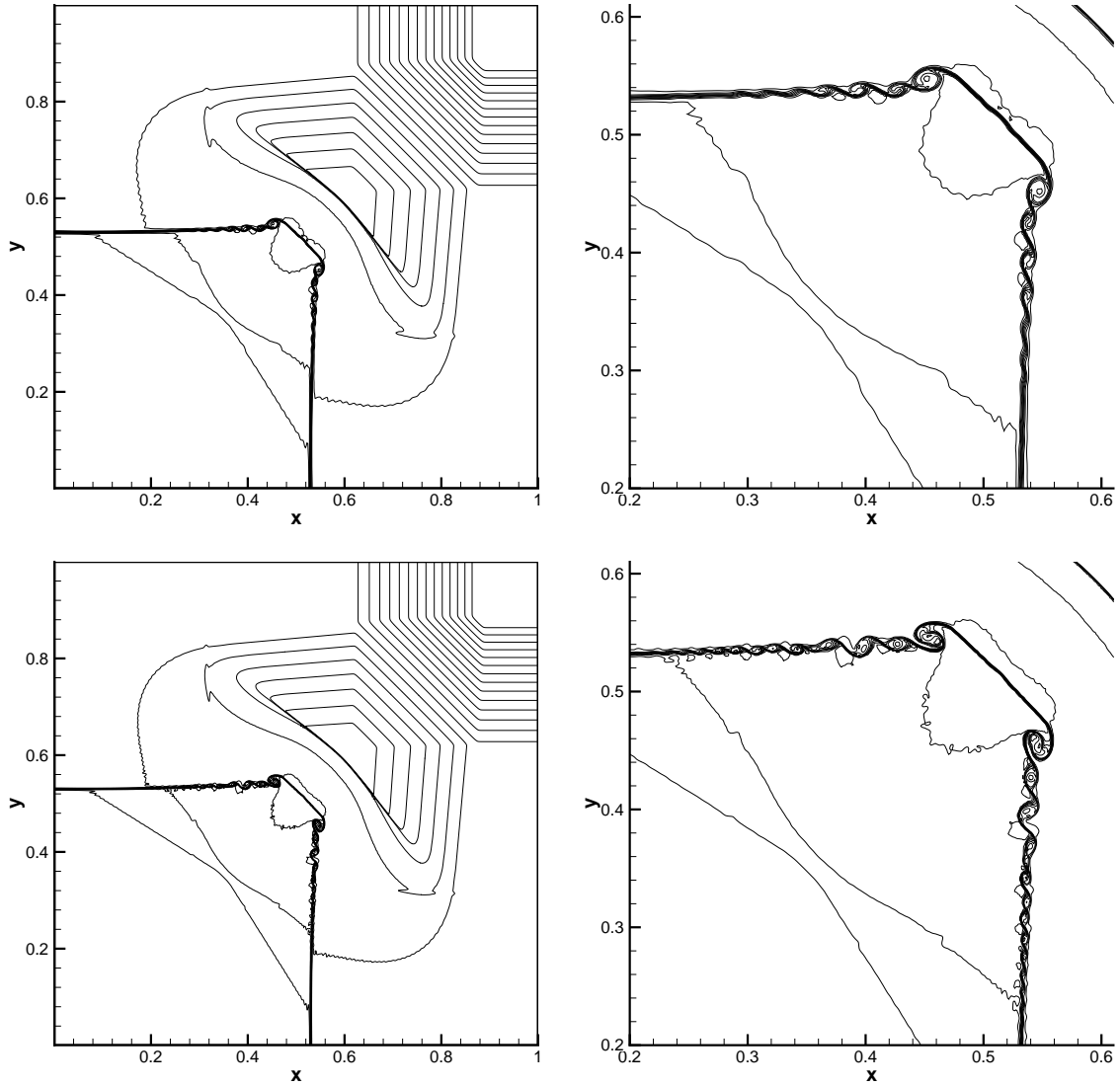


Figure 5: The density distribution for the second two-dimensional Riemann problem at  $t = 0.25$  with  $600 \times 600$  (top) and  $1000 \times 1000$  (bottom) mesh points.

order scheme. Since the fourth-order GKS has three Gauss points for flux evaluation and two stages, the three times computational time difference means that the reconstruction makes great contribution to the computational cost as well, because in terms of reconstruction cost the fourth-order scheme only takes about two times of computational cost of second-order scheme. However, in order to get the same accuracy as that of the fourth-order scheme, the second-order method needs refine the mesh, at least once. In the two-dimensional calculation, the computational cost for one mesh refinement will be increased by 8 times. Therefore, the fourth-order scheme is more efficient than the second order method. Since higher-order scheme does have advantages in comparison with lower order method, it is

worth to construct the two-stage fifth-order GKS from the third-order GKS flux function, see Appendix. Besides the computational cost, another important property of the fourth-order GKS is its accuracy and robustness. As tested in the above cases and all cases in the following, it clearly indicates that the fourth-order scheme is very accurate and is as robust as the second-order one. The accuracy of the scheme is closely related to the higher-order gas evolution model, multi-dimensionality for the inclusion of both normal and tangential derivatives around a cell interface, and the unified treatment of the inviscid and viscous terms. A fundamental reason for the robustness of the scheme is its first-order relaxation model, where the system is fully hyperbolic with local source term.

#### 4.4. Shock vortex interaction

The interaction between a stationary shock and a vortex for the inviscid flow [14] is presented. The computational domain is taken to be  $[0, 2] \times [0, 1]$ . A stationary Mach 1.1 shock is positioned at  $x = 0.5$  and normal to the  $x$ -axis. The left upstream state is  $(\rho, U, V, p) = (Ma^2, \sqrt{\gamma}, 0, 1)$ , where  $Ma$  is the Mach number. A small vortex is obtained through a perturbation on the mean flow with the velocity  $(U, V)$ , temperature  $T = p/\rho$ , and entropy  $S = \ln(p/\rho^\gamma)$ . The perturbation is expressed as

$$\begin{aligned}(\delta U, \delta V) &= \kappa \eta e^{\mu(1-\eta^2)} (\sin \theta, -\cos \theta), \\ \delta T &= -\frac{(\gamma-1)\kappa^2}{4\mu\gamma} e^{2\mu(1-\eta^2)}, \delta S = 0,\end{aligned}$$

where  $\eta = r/r_c$ ,  $r = \sqrt{(x-x_c)^2 + (y-y_c)^2}$ , and  $(x_c, y_c) = (0.25, 0.5)$  is the center of the vortex. Here  $\kappa$  indicates the strength of the vortex,  $\mu$  controls the decay rate of the vortex, and  $r_c$  is the critical radius for which the vortex has the maximum strength. In the computation,  $\kappa = 0.3$ ,  $\mu = 0.204$ , and  $r_c = 0.05$ . The reflected boundary conditions are used on the top and bottom boundaries. The pressure distributions with mesh size  $\Delta x = \Delta y = 1/200$  at  $t = 0, 0.3, 0.6$  and  $0.8$  are shown in Fig.6. By  $t = 0.8$ , one branch of the shock bifurcations has reached the top boundary and been reflected. The reflection is well captured. The detailed density distributions along the center horizontal line with mesh size  $\Delta x = \Delta y = 1/50, 1/100$  and  $1/200$  at  $t = 0.8$  are shown in Fig.7. The accuracy of the scheme is well demonstrated.

#### 4.5. Double Mach reflection problem

This problem was extensively studied by Woodward and Colella [33] for the inviscid flow. The computational domain is  $[0, 4] \times [0, 1]$ , and a solid wall lies at the bottom of the computational domain starting from  $x = 1/6$ . Initially a right-moving Mach 10 shock is positioned at  $(x, y) = (1/6, 0)$ , and makes a  $60^\circ$  angle with the  $x$ -axis. The initial pre-shock and post-shock conditions are

$$\begin{aligned}(\rho, U, V, p) &= (8, 4.125\sqrt{3}, -4.125, 116.5), \\ (\rho, U, V, p) &= (1.4, 0, 0, 1).\end{aligned}$$



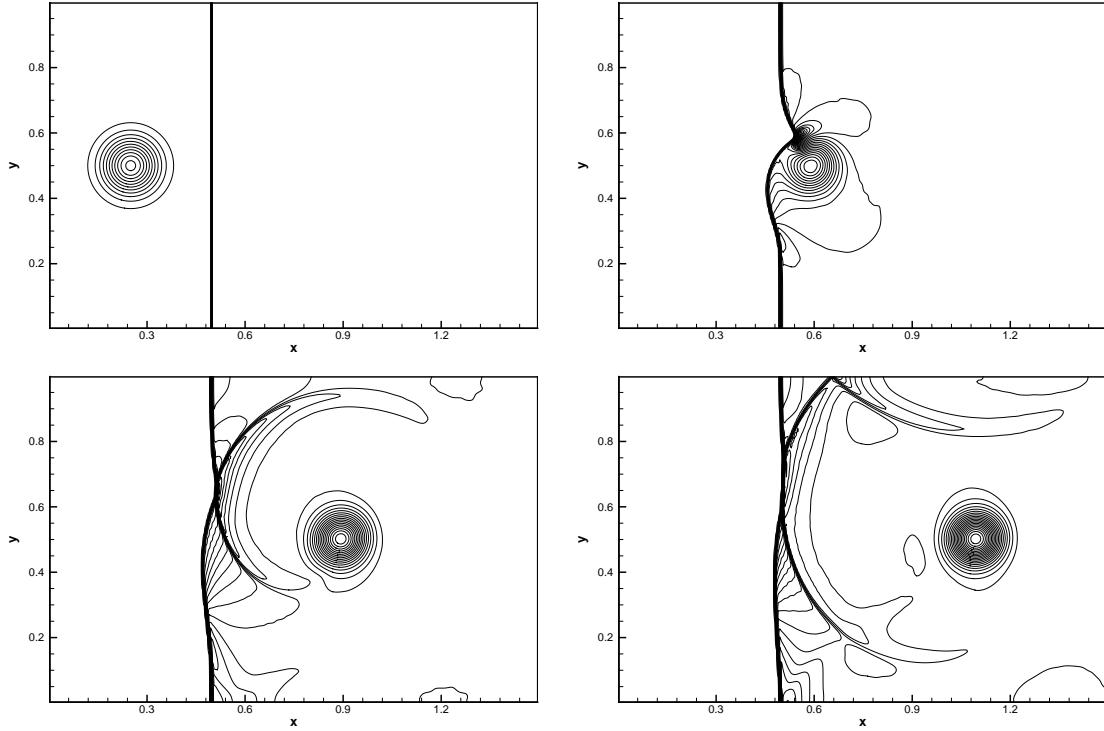


Figure 6: Shock vortex interaction: the pressure distribution at  $t = 0, 0.3, 0.6$  and  $0.8$  with mesh size  $\Delta x = \Delta y = 1/200$ .

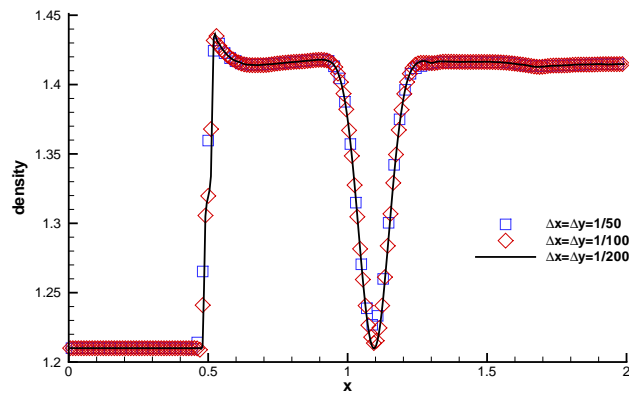


Figure 7: Shock vortex interaction: the density distribution at  $t = 0.8$  along the horizontal symmetric line  $y = 0.5$  with mesh size  $\Delta x = \Delta y = 1/50, 1/100$  and  $1/200$ .

The reflective boundary condition is used at the wall, while for the rest of bottom boundary, the exact post-shock condition is imposed. At the top boundary, the flow values are set to describe the exact motion of the Mach 10 shock. The density distributions with  $720 \times 240$  and  $1440 \times 480$  uniform mesh points at  $t = 0.2$  are shown in Fig.8 and Fig.9, respectively. The current scheme resolves the flow structure under the triple Mach stem clearly. The

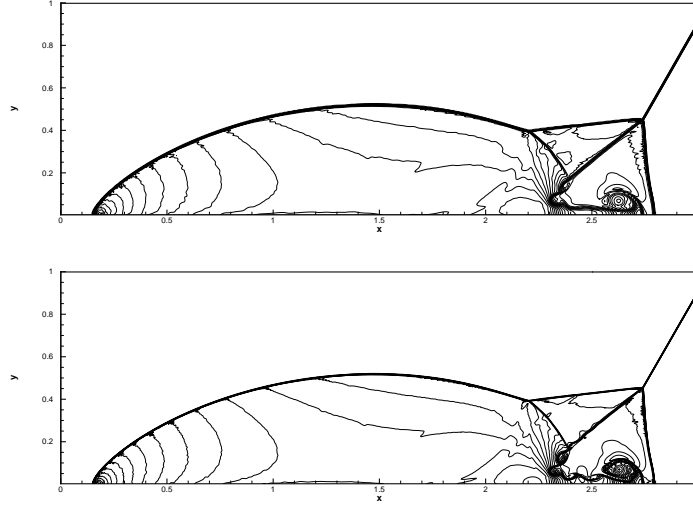


Figure 8: Double Mach reflection: density contours with the  $720 \times 240$  (top) and  $1440 \times 480$  (bottom) mesh points.

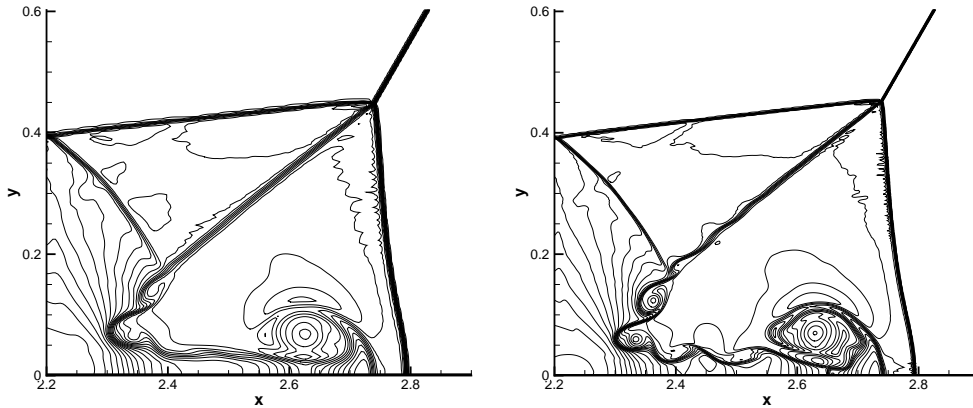


Figure 9: Double Mach reflection: enlarged density distributions around the triple point with the  $720 \times 240$  (left) and  $1440 \times 480$  (right) mesh points.

amplitude of the oscillation of the slip line from the triple point is not as large as that from many other higher-order schemes, because the GKS is intrinsically solving the NS equations and the physical dissipation will stabilize the shear instability.

#### 4.6. Hypersonic flow past a cylinder

In this case, the hypersonic flows impinging on a unit cylinder are tested to validate robustness of the current scheme. The first one is the inviscid flow, which were also studied in [19] as comparison between GRP and GKS. This problem is initialized by the flow moving towards to a cylinder with different Mach numbers. The reflective boundary condition is imposed on the surface of cylinder, and the outflow boundary condition is set on the right boundary. In the computation, the  $60 \times 100$  mesh points are used, which is

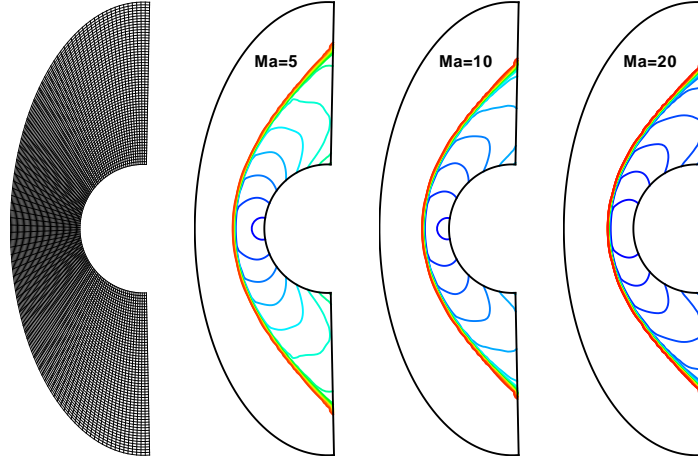


Figure 10: Hypersonic inviscid flow past a cylinder: the Mach number distributions for the flow with Mach number  $Ma = 5, 10$  and  $20$ .

shown in Fig.10. The Mach number distributions for the flows with  $Ma = 5, 10$ , and  $20$  are also presented in Fig.10, which show that the current scheme can capture strong shocks very well without carbuncle phenomenon [27]. The robustness of the scheme is well validated.

The viscous and heat conducting case at high Mach number is also tested. The flow condition is given as  $Ma_\infty = 8.03$ ,  $T_\infty = 124.94K$  for the far field, the wall temperature is  $T_W = 294.44K$ , and the Reynolds number is  $Re = 1.835 \times 10^5$  with cylinder radius and the far field flow parameters. This test case is taken from the experiment done by Wieting [32]. A non-uniform mesh of  $60 \times 160$  cells is used with the near-wall cell width of  $1/2000$  to resolve the boundary layer. The mesh, pressure, temperature, and Mach number distributions are given in Fig.11. The pressure and heat flux along the cylindrical surface are presented in Fig.12, where the numerical results agree well with the experimental data [32].

#### 4.7. Laminar boundary layer

A laminar boundary layer is tested over a flat plate. The Mach number of the free-stream is  $Ma = 0.15$  and the Reynolds number is  $Re = U_\infty L/\nu = 10^5$ ,  $\nu$  is the viscous coefficient. The non-slip adiabatic boundary condition at the plate is used and a symmetric condition is imposed at the bottom boundary before the flat plate. The non-reflecting boundary condition based on the Riemann invariants is adopted for the other boundaries. A uniform mesh  $260 \times 90$  points is adopted with  $\Delta x = \Delta y = 1/200$ , including  $60 \times 90$  mesh points before the plate. At steady state, the non-dimensional  $U$  and  $V$  velocity at different locations are presented in Fig.13, as well as the wall friction coefficient. In all locations, the numerical solutions match with the exact Blasius solution very well. At the upstream location, the boundary layer profile can be accurately captured with only four grid points within the layer.

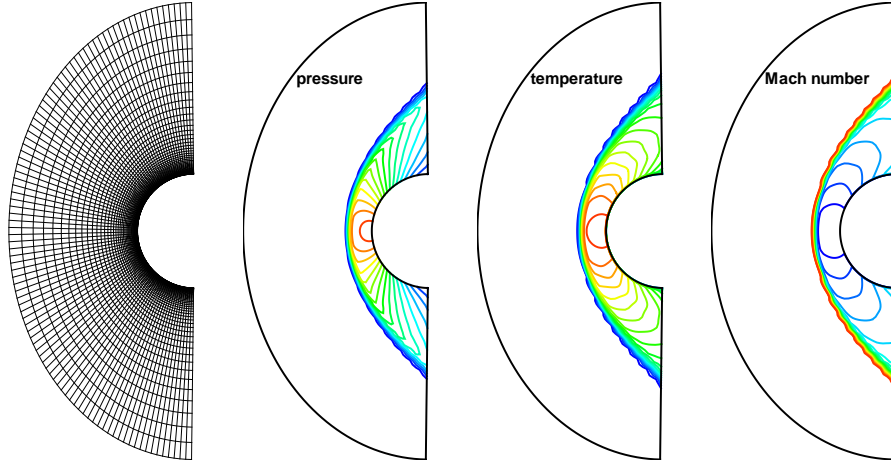


Figure 11: Hypersonic viscous flow past a cylinder with  $Ma = 8.03$ : the mesh, pressure, temperature, and Mach number distributions.

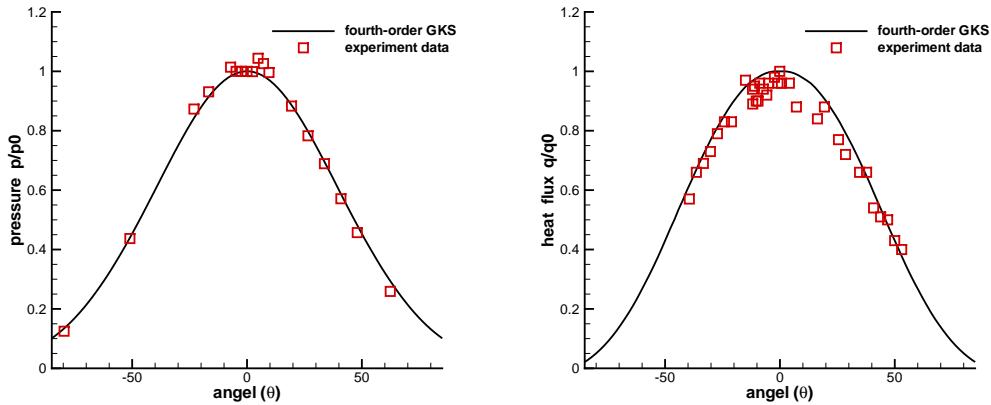


Figure 12: Hypersonic viscous flow past a cylinder with  $Ma = 8.03$ . Comparison of the computed pressure and heat flux along the cylindrical surface with the experimental data [32].

#### 4.8. Lid-driven cavity flow

In order to further test the scheme in the capturing of vortex flow, the lid-driven cavity problem is one of the most important benchmarks for validating incompressible low speed Navier-Stokes flow solvers. The fluid is bounded by a unit square and is driven by a uniform translation of the top boundary. In this case, the flow is simulated with Mach number  $Ma = 0.15$  and all boundaries are isothermal and nonslip. The computational domain  $[0, 1] \times [0, 1]$  is covered with  $65 \times 65$  mesh points. Numerical simulations are conducted for two different Reynolds numbers, i.e.,  $Re = 1000$  and  $3200$ . The streamlines in Fig.14, the  $U$ -velocities along the center vertical line, and  $V$ -velocities along the center horizontal line, are shown in Fig.15. The benchmark data [9] for  $Re = 1000$  and  $3200$  are also presented, and the simulation results match well with these benchmark data. The higher-order accuracy

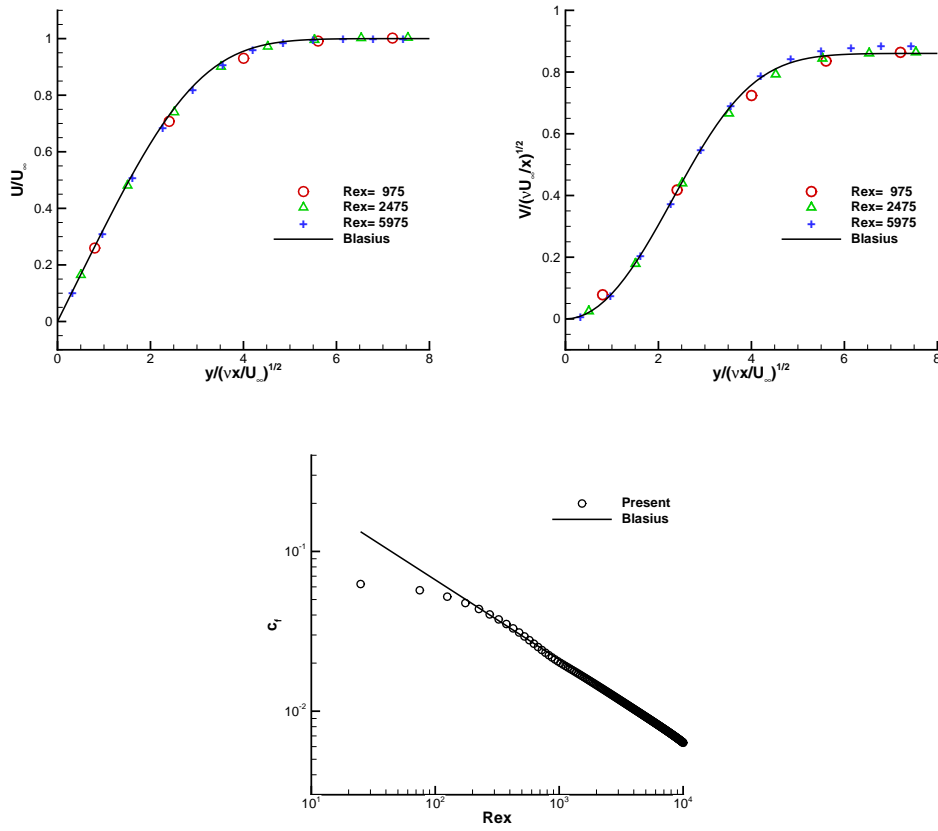


Figure 13: Laminar boundary layer: the  $U$  and  $V$  velocity profiles at different locations and wall friction coefficient distribution.

of the scheme is clearly demonstrated from the Reynolds number 3200 case, where only 65 uniform mesh points are used in each direction.

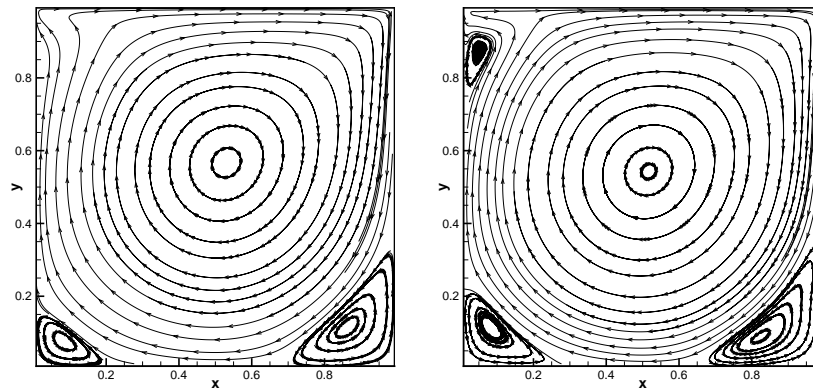


Figure 14: Lid-driven cavity flow: the streamlines with  $65 \times 65$  mesh points from the fourth-order GKS at  $Re = 1000$  (left) and 3200 (right).

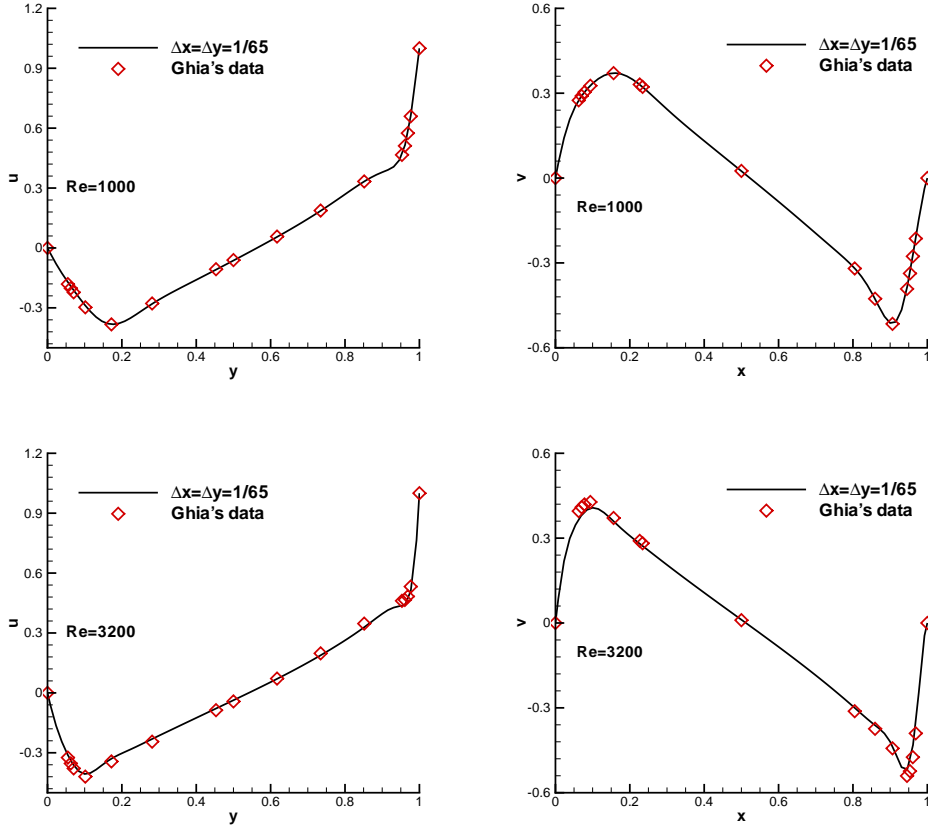


Figure 15: Lid-driven cavity flow:  $U$ -velocity along vertical centerline line and  $V$ -velocity along horizontal centerline with 65 mesh points in each direction from the fourth-order GKS at  $Re = 1000$  and  $3200$ .

#### 4.9. Viscous shock tube problems

This problem was introduced to test the performances of different schemes for viscous flows [7]. In this case, an ideal gas is at rest in a two-dimensional unit box  $[0, 1] \times [0, 1]$ . A membrane located at  $x = 0.5$  separates two different states of the gas and the dimensionless initial states are

$$(\rho, U, p) = \begin{cases} (120, 0, 120/\gamma), & 0 < x < 0.5, \\ (1.2, 0, 1.2/\gamma), & 0.5 < x < 1, \end{cases}$$

where  $\gamma = 1.4$  and Prandtl number  $Pr = 0.73$ .

Scheme	AUSMPW+	M-AUSMPW+	fourth-order GKS
height	0.163	0.168	0.171

Table 5: Comparison of the heights of primary vortex among gas kinetic scheme and other reference methods [15] for the reflecting shock-boundary layer interaction with  $\Delta x = \Delta y = 1/500$ .

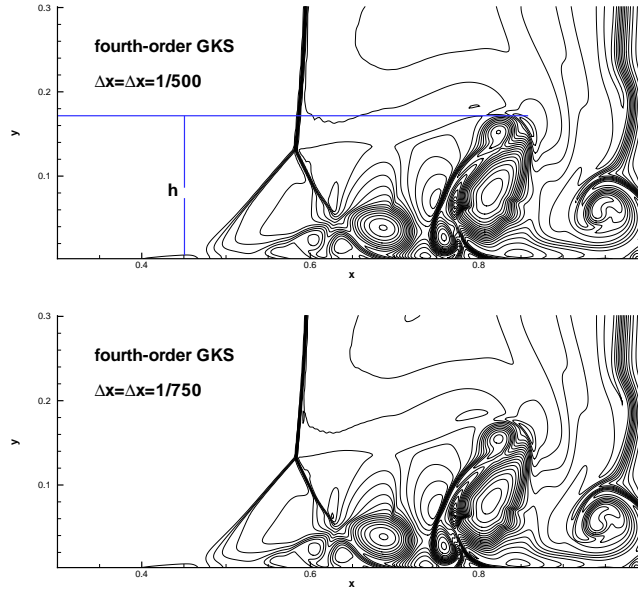


Figure 16: Reflecting shock-boundary layer interaction: density distributions at  $t = 1$  with  $Re = 200$  from the fourth-order GKS with  $\Delta x = \Delta y = 1/500, 1/750$ .

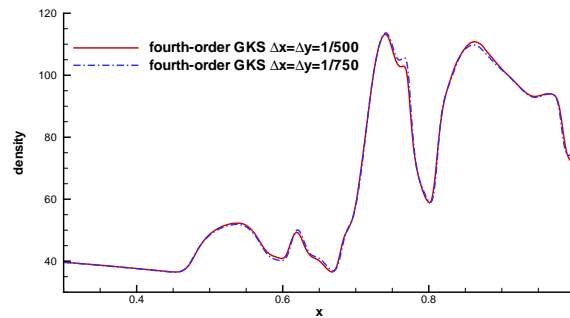


Figure 17: Reflecting shock-boundary layer interaction: density distribution along the lower wall with different mesh sizes for  $Re = 200$ .

The membrane is removed at time zero and wave interaction occurs. A shock wave, followed by a contact discontinuity, moves to the right with Mach number  $Ma = 2.37$  and reflects at the right end wall. After the reflection, it interacts with the contact discontinuity. The contact discontinuity and shock wave interact with the horizontal wall and create a thin boundary layer during their propagation. The solution will develop complex two-dimensional shock/shear/boundary-layer interactions. This case is tested in the computational domain  $[0, 1] \times [0, 0.5]$ , a symmetric boundary condition is used on the top boundary  $x \in [0, 1], y = 0.5$ , and non-slip boundary condition, and adiabatic condition for temperature are imposed at solid wall boundaries. The case with  $Re = 200$  is tested first. The density distributions are presented in Fig.16 with two different mesh resolutions. The results match well with

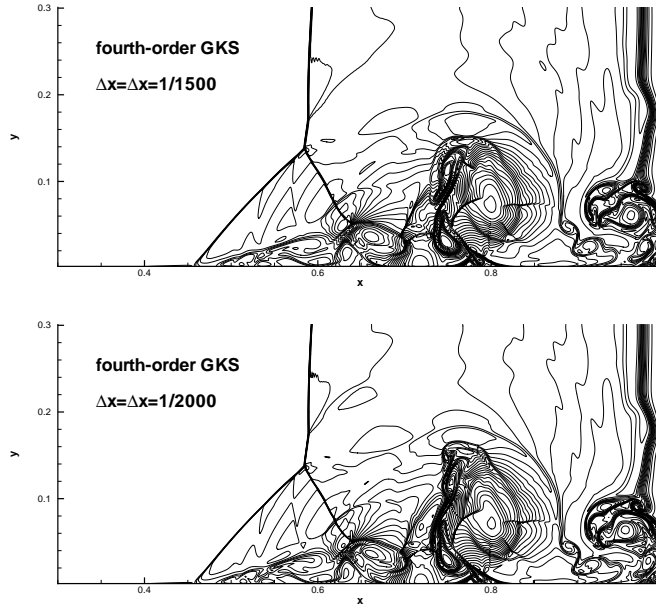


Figure 18: Reflecting shock-boundary layer interaction. The density distribution at  $t = 1$  with  $Re = 1000$  with  $\Delta x = \Delta y = 1/1500$  and  $1/2000$ .

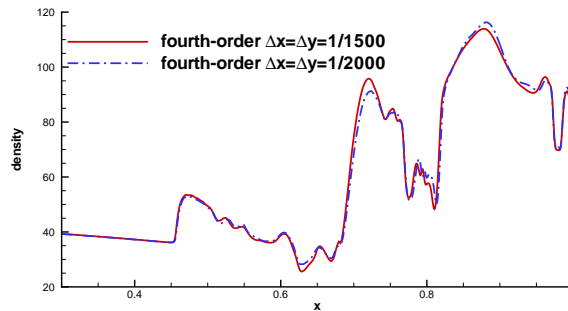


Figure 19: Reflecting shock-boundary layer interaction: density distribution along the lower wall with different mesh sizes for  $Re = 1000$ .

each other. The density profiles along the lower wall with  $Re = 200$  are also presented in Fig.19. A mesh-convergent solution is observed for  $Re = 200$ . As shown in Table.5, the height of primary vortex predicted by the current scheme agrees well with the reference data [15]. For the case with  $Re = 1000$ , the flow structure becomes more complicated. The density distributions from the current scheme are given in Fig.18, and the density profiles along the lower wall are presented in Fig.19 with the mesh size  $\Delta x = \Delta y = 1/1500$  and  $1/2000$ . The flow structure is complicated, and the mesh convergence is basically obtained with the mesh size decreasing to  $1/1500$ . The current results agree well with the reference data very well. More studies for this problem can be found in [7].



## 5. Conclusion

In this paper, based on the two-stage time stepping method a fourth-order gas-kinetic scheme is proposed for both inviscid and viscous flow computations. With the fifth-order WENO reconstruction, a GKS with a fifth order accuracy in space and a fourth order accuracy in time is developed. In comparison with the classical methods based on the first-order Riemann solver, for a fourth-order accuracy in time the current GKS only uses two stages instead of four stages in the conventional methods. Therefore, the current GKS should be much more efficient than these higher-order methods based on the Riemann solutions, especially for the NS solutions. The current finite volume scheme can use a CFL number on the order of 0.5. The further development of the GKS to even higher-order accuracy can be achieved with the inclusion of the second-order time derivative of the flux function, such as the fifth-order scheme presented in the Appendix. The fourth-order GKS not only has the expected order of accuracy for the smooth flow, but also has favorable shock capturing property for the discontinuous solutions. Most importantly, the numerical tests clearly demonstrate that the current fourth-order scheme is as robust as the second-order one.

By taking advantage of the time-accurate gas evolution model in the flux evaluation, an efficient and accurate fourth-order gas-kinetic scheme has been constructed. The advantage of the time accurate evolution model can be further explored for the construction of higher-order compact schemes [25, 26], where not only the flux at the cell interface, the conservative flow variables at the cell interface can be updated as well to construct compact stencils for the flow reconstruction in the next time level. Based on the current study, we can conclude that the adaptation of a higher-order gas evolution model for the flux evaluation has an indispensable advantage in the development of higher-order schemes. The real bottleneck which hinders the progress for the development of higher-order accurate and robust schemes for the compressible flows is due to the use of first-order Riemann solver.

## Acknowledgements

The research of K. Xu is supported by Hong Kong Research Grant Council (620813, 16211014, 16207715) and HKUST research fund (PROVOST13SC01, IRS15SC29, SBI14SC11). The research of Q. Li is partially supported by NSFC (11172154). The work of J. Li is supported by NSFC (91130021, 11371063), and the doctoral program from the Education Ministry of China (20130003110004).

## Appendix: Extension to higher order

The key point for developing a two-stage fourth-order temporal accurate schemes is the use of a time-dependent flux function. The third-order GRP and GKS have both first- and second-order time derivatives in the flux function [28, 21, 24, 25]. Thus, with a two-stage temporal discretization and the third-order GRP and GKS flux solvers, it is possible to develop schemes with fifth-order accuracy in time.

We consider the time-dependent equation Eq.(1) with the initial condition Eq.(2). Introducing an intermediate state at  $t_* = t_n + A\Delta t$ ,

$$\mathbf{w}^* = \mathbf{w}^n + A\Delta t\mathcal{L}(\mathbf{w}^n) + \frac{1}{2}A^2\Delta t^2\frac{\partial}{\partial t}\mathcal{L}(\mathbf{w}^n) + \frac{1}{6}A^3\Delta t^3\frac{\partial^2}{\partial t^2}\mathcal{L}(\mathbf{w}^n), \quad (17)$$

we will have  $\mathcal{L}(\mathbf{w}^*)$ ,  $\frac{\partial}{\partial t}\mathcal{L}(\mathbf{w}^*)$  and  $\frac{\partial^2}{\partial t^2}\mathcal{L}(\mathbf{w}^*)$  at  $t_*$ . Then, the update scheme can be written as

$$\begin{aligned} \mathbf{w}^{n+1} = & \mathbf{w}^n + \Delta t(B_0\mathcal{L}(\mathbf{w}^n) + B_1\mathcal{L}(\mathbf{w}^*)) + \frac{1}{2}\Delta t^2(C_0\frac{\partial}{\partial t}\mathcal{L}(\mathbf{w}^n) + C_1\frac{\partial}{\partial t}\mathcal{L}(\mathbf{w}^*)) \\ & + \frac{1}{6}\Delta t^3(D_0\frac{\partial^2}{\partial t^2}\mathcal{L}(\mathbf{w}^n) + D_1\frac{\partial^2}{\partial t^2}\mathcal{L}(\mathbf{w}^*)). \end{aligned} \quad (18)$$

It can be proved that Eq.(17) and Eq.(18) can provide a fifth-order temporal accurate approximation to the solution  $\mathbf{w}(t)$  at  $t = t_n + \Delta t$  with the following coefficients

$$A = \frac{2}{5}, B_0 = 1, B_1 = 0, C_0 = 1, C_1 = 0, D_0 = \frac{3}{8}, D_1 = \frac{5}{8}. \quad (19)$$

To prove this proposition, the following equation needs to be satisfied, using the same approach as in [18],

$$\mathbf{w}^{n+1} = \mathbf{w}^n + \int_{t_n}^{t_n+\Delta t} \mathcal{L}(\mathbf{w}(t))dt + \mathcal{O}(\Delta t^6).$$

According to the Taylor expansion of the operator  $\mathcal{L}$  at  $t_n$ , the integral can be expressed as

$$\int_{t_n}^{t_n+\Delta t} \mathcal{L}(\mathbf{w}(t))dt = \Delta t\mathcal{L} + \frac{\Delta t^2}{2}\frac{\partial \mathcal{L}}{\partial t} + \frac{\Delta t^3}{6}\frac{\partial^2 \mathcal{L}}{\partial t^2} + \frac{\Delta t^4}{24}\frac{\partial^3 \mathcal{L}}{\partial t^3} + \frac{\Delta t^5}{120}\frac{\partial^4 \mathcal{L}}{\partial t^4} + \mathcal{O}(\Delta t^6), \quad (20)$$

where the time derivatives for the operator  $\mathcal{L}$  can be given by the chain rule, for example

$$\frac{\partial \mathcal{L}}{\partial t} = \mathcal{L}_{\mathbf{w}}\mathcal{L}, \quad \frac{\partial^2 \mathcal{L}}{\partial t^2} = \mathcal{L}_{\mathbf{w}}^2\mathcal{L} + \mathcal{L}_{\mathbf{w}\mathbf{w}}\mathcal{L}^2, \dots$$

Denote  $\mathcal{G}(\mathbf{w}) = \frac{\partial}{\partial t}\mathcal{L}(\mathbf{w})$  and  $\mathcal{H}(\mathbf{w}) = \frac{\partial^2}{\partial t^2}\mathcal{L}(\mathbf{w})$ , and expand  $\mathcal{L}(\mathbf{w})$ ,  $\mathcal{G}(\mathbf{w})$  and  $\mathcal{H}(\mathbf{w})$  in the neighboring of  $\mathbf{u}^*$  to the corresponding order, we have

$$\begin{aligned} \mathcal{L}(\mathbf{w}^*) &= \mathcal{L}(\mathbf{w}^n) + \mathcal{L}_{\mathbf{w}}(\mathbf{w}^* - \mathbf{w}^n) + \frac{\mathcal{L}_{\mathbf{w}\mathbf{w}}}{2}(\mathbf{w}^* - \mathbf{w}^n)^2 + \frac{\mathcal{L}_{\mathbf{w}\mathbf{w}\mathbf{w}}}{6}(\mathbf{w}^* - \mathbf{w}^n)^3 + \frac{\mathcal{L}_{\mathbf{w}\mathbf{w}\mathbf{w}\mathbf{w}}}{24}(\mathbf{w}^* - \mathbf{w}^n)^4, \\ \mathcal{G}(\mathbf{w}^*) &= \mathcal{G}(\mathbf{w}^n) + \mathcal{G}_{\mathbf{w}}(\mathbf{w}^* - \mathbf{w}^n) + \frac{\mathcal{G}_{\mathbf{w}\mathbf{w}}}{2}(\mathbf{w}^* - \mathbf{w}^n)^2 + \frac{\mathcal{G}_{\mathbf{w}\mathbf{w}\mathbf{w}}}{6}(\mathbf{w}^* - \mathbf{w}^n)^3, \\ \mathcal{H}(\mathbf{w}^*) &= \mathcal{H}(\mathbf{w}^n) + \mathcal{H}_{\mathbf{w}}(\mathbf{w}^* - \mathbf{w}^n) + \frac{\mathcal{H}_{\mathbf{w}\mathbf{w}\mathbf{w}}}{2}(\mathbf{w}^* - \mathbf{w}^n)^2, \end{aligned}$$

where obvious higher order terms are ignored,  $\mathbf{w}^*$  is given by Eq.(17). Substituting  $\mathcal{L}(\mathbf{w}^*)$ ,  $\mathcal{G}(\mathbf{w}^*)$ ,  $\mathcal{H}(\mathbf{w}^*)$  into Eq.(18) and comparing the coefficients of Eq.(20), a system of equations will be obtained, and Eq.(19) is its unique solution for this system.

To develop the gas-kinetic scheme with fifth-order temporal accuracy, the time-dependent flux should be approximated by the quadratic function, which is expressed as follows

$$F_{i+1/2}(W^n, t) = F_{i+1/2}^n + \partial_t F_{i+1/2}^n t + \frac{1}{2} \partial_{tt} F_{i+1/2}^n t^2. \quad (21)$$

In a time step, the coefficients  $F_{i+1/2}^n$ ,  $\partial_t F_{i+1/2}^n$  and  $\partial_{tt} F_{i+1/2}^n$  can be determined as follows

$$\begin{aligned} F_{i+1/2} \Delta t + \frac{1}{2} \partial_t F_{i+1/2} \Delta t^2 + \frac{1}{6} \partial_{tt} F_{i+1/2} \Delta t^3 &= \mathbb{F}_{i+1/2}(W^n, \Delta t), \\ \frac{2}{3} F_{i+1/2} \Delta t + \frac{2}{9} \partial_t F_{i+1/2} \Delta t^2 + \frac{4}{81} \partial_{tt} F_{i+1/2} \Delta t^3 &= \mathbb{F}_{i+1/2}(W^n, 2\Delta t/3), \\ \frac{1}{3} F_{i+1/2} \Delta t + \frac{1}{18} \partial_t F_{i+1/2} \Delta t^2 + \frac{1}{162} \partial_{tt} F_{i+1/2} \Delta t^3 &= \mathbb{F}_{i+1/2}(W^n, \Delta t/3), \end{aligned}$$

where

$$\mathbb{F}_{i+1/2}(W^n, \delta) = \int_{t_n}^{t_n+\delta} \int u f(x_{i+1/2}, t, u, v, \xi) du d\xi dt.$$

The formulation for the gas distribution  $f(x_{i+1/2}, t, u, v, \xi)$  can be found in [21, 24, 25]. By solving the linear system, all coefficients can be determined.

## References

- [1] M. Ben-Artzi, J. Falcovitz, A second-order Godunov-type scheme for compressible uid dynamics, J. Comput. Phys. 55 (1984), 1-32.
- [2] M. Ben-Artzi, J. Li, G. Warnecke, A direct Eulerian GRP scheme for compressible uid ows, J. Comput. Phys. 218 (2006), 19-43.
- [3] M. Ben-Artzi, J. Li, Hyperbolic conservation laws: Riemann invariants and the generalized Riemann problem, Numerische Mathematik, 106 (2007) 369-425.
- [4] P.L. Bhatnagar, E.P. Gross, M. Krook, A Model for Collision Processes in Gases I: Small Amplitude Processes in Charged and Neutral One-Component Systems, Phys. Rev. 94 (1954) 511-525.
- [5] S. Chapman, T.G. Cowling, The Mathematical theory of Non-Uniform Gases, third edition, Cambridge University Press, (1990).
- [6] B. Cockburn, C. W. Shu, Runge-Kutta Discontinuous Galerkin Methods for Convection-Dominated Problems, Journal of Scientific Computing, Vol. 16 (2001), No. 3, pp. 173-261.
- [7] V. Daru, C. Tenaud, Numerical simulation of the viscous shock tube problem by using a high resolution monotonicity-preserving scheme, Computers & Fluids 38 (2009) 664-676.
- [8] M. Dumbser, D.S. Balsara, E.F. Toro, C.D. Munz, A unified framework for the construction of one-step finite volume and discontinuous Galerkin schemes on unstructured meshes, J. Comput. Phys. 227 (2008) 8209-8253.
- [9] U. Ghia, K. N. Ghia, C.T Shin, High-Re solutions for incompressible flow using the Navier-Stokes equations and a multigrid method, J. Comput. Phys. 48 (1982) 387-411.
- [10] S. Gottlieb, C. W. Shu, Total variation diminishing runge-kutta schemes, Mathematics of computation, 67 (1998) 73-85.

- [11] E. Han, J. Li and H. Tang, Accuracy of the adaptive GRP scheme and the simulation of 2-D Riemann problem for compressible Euler equations, *Comm. Comput. Phys.*, Vol. 10 (2011), 577-606.
- [12] A. Harten, B. Engquist, S. Osher and S. R. Chakravarthy, Uniformly high order accurate essentially non-oscillatory schemes, III. *J. Comput. Phys.* 71 (1987) 231-303.
- [13] S. Li and F. Xiao, High order multi-moment constrained finite volume method. Part I: Basic formulation, *J. Comput. Phys.* 228 (2009), pp. 3669C3707.
- [14] G.S. Jiang, C. W. Shu, Efficient implementation of Weighted ENO schemes, *J. Comput. Phys.* 126 (1996) 202-228.
- [15] K.H. Kim, C. Kim, Accurate, efficient and monotonic numerical methods for multi-dimensional compressible flows Part I: Spatial discretization, *J. Comput. Phys.* 208 (2005) 527-569.
- [16] G. Kumar, S.S. Girimaji, J. Kerimo, WENO-enhanced gas-kinetic scheme for direct simulations of compressible transition and turbulence, *J. Comput. Phys.* 234 (2013) 499-523.
- [17] P. D. Lax, X.D. Liu, Solution of two-dimensional Riemann problems of gas dynamics by positive schemes, *SIAM J. Sci. Comput.* 19 (1998) 319-340.
- [18] J. Li, Z. Du, A two-stage fourth order time-accurate discretization for Lax-Wendroff type flow solvers I. hyperbolic conservation laws, preprint, <http://arxiv.org/abs/1512.03664>, 2015.
- [19] J. Li, Q. Li, K. Xu, Comparison of the generalized Riemann solver and the gas-kinetic scheme for inviscid compressible flow simulations, *J. Comput. Phys.* 230 (2011) 5080-5099.
- [20] J. Li, T. Zhang and S. Yang, *The Two-dimensional Riemann Problem in Gas Dynamics*, Pitman Monographs and Surveys in Pure and Applied Mathematics 98, Longman Scientific & Technical, Harlow (1998).
- [21] Q. Li, K. Xu, S. Fu, A high-order gas-kinetic Navier-Stokes flow solver, *J. Comput. Phys.* 229 (2010) 6715-6731.
- [22] N. Liu and H.Z. Tang, A high-order accurate gas-kinetic scheme for one- and two-dimensional flow simulation, *Commun. Comput. Phys.*, 15 (2014), 911-943.
- [23] X.D. Liu, S. Osher, T. Chan, Weighted essentially non-oscillatory schemes, *J. Comput. Phys.* 115 (1994) 200-212.
- [24] J. Luo, K. Xu, A high-order multidimensional gas-kinetic scheme for hydrodynamic equations, *SCIENCE CHINA Technological Sciences*, 56 (2013) 2370-2384.
- [25] L. Pan, K. Xu, A compact third-order gas-kinetic scheme for compressible Euler and Navier-Stokes equations, *Commun. Comput. Phys.* 18 (2015) 985-1011.
- [26] L. Pan, K. Xu, A third-order compact gas-kinetic scheme on unstructured meshes for compressible Navier-Stokes solutions, arXiv:1602:00394v1 [math.NA] February (2016).
- [27] M. Pandolfi, and D. D'Ambrosio, Numerical Instabilities in Upwind Methods: Analysis and Cures for the "Carbuncle" Phenomenon, *J. Comput. Phys.* 166 (2001) 271-301.
- [28] J. Qian, J. Li and S. Wang, The generalized Riemann problems for compressible fluid flows: Towards high order, *J. Comput. Phys.* 259 (2014) 358-389.
- [29] X. Ren, K. Xu, W. Shyy, C. Gu, A multi-dimensional high-order discontinuous Galerkin method based on gas kinetic theory for viscous flow computations, *J. Comput. Phys.* 292 (2015) 176-193.
- [30] C.W. Shu and S. Osher, Efficient implementation of essentially nonoscillatory shock-capturing schemes II, *J. Comput. Phys.*, 83 (1989), pp. 32-78.
- [31] E. Toro, *Riemann Solvers and Numerical Methods for Fluid Dynamics*, Springer, (1997).
- [32] A.R. Wieting, Experimental study of shock wave interface heating on a cylindrical leading edge, No. NASA TM-100484 1987.
- [33] P. Woodward and P. Colella, Numerical simulations of two-dimensional fluid flow with strong shocks, *J. Comput. Phys.* 54 (1984) 115-173.
- [34] K. Xu, A gas-kinetic BGK scheme for the Navier-Stokes equations and its connection with artificial dissipation and Godunov method, *J. Comput. Phys.* 171 (2001) 289-335.
- [35] K. Xu, Super-Burnett solutions for Poiseuille flow, *Physics of Fluids*, Vol. 15 (2003), pp. 2077-2080.
- [36] K. Xu, *Direct modeling for computational fluid dynamics: construction and application of unified gas kinetic schemes*, World Scientific (2015).

- [37] K. Xu, Z.H. Li, Microchannel flow in the slip regime: gas-kinetic BGK-Burnett solutions, *J. Fluid Mech.* 513 (2004) 87-110.